Research Square

Preprints are preliminary reports that have not undergone peer review.
They should not be considered conclusive, used to inform clinical practice,
or referenced by the media as validated information.

Stable Phenanthrene-Fused 1,2,4-Triazinyl Radicals with Ultra-narrow Electrochemical Gap Enabled by Attenuated Fusion-Ring Aromaticity

Ying Wang

ywang1@bnu.edu.cn

Beijing Normal University https://orcid.org/0000-0002-7015-7228

Weijie Guo

Beijing Normal University

Sijia Yue

Beijing Normal University

Ran Duan

Institute of Chemistry, Chinese Academy of Sciences

Zhibo Yuan

Beijing Normal University

Yuqing Yao

Beijing Normal University

Hua Jiang

Beijing Normal University https://orcid.org/0000-0002-9917-2683

Jing Guo

Beijing Normal University https://orcid.org/0000-0001-8606-001X

Andrzej Rajca

University of Nebraska–Lincoln https://orcid.org/0000-0002-8856-1536

Article

Keywords:

Posted Date: June 4th, 2026

DOI: https://doi.org/10.21203/rs.3.rs-9661849/v1

License: This work is licensed under a Creative Commons Attribution 4.0 International License.
Read Full License

Additional Declarations: There is **NO** Competing Interest.

Stable Phenanthrene-Fused 1,2,4-Triazinyl Radicals with Ultra-narrow Electrochemical Gap Enabled by Attenuated Fusion-Ring Aromaticity

Weijie Guo,[a] Sijia Yue,[a] Ran Duan,[c] Zhibo Yuan,[a] Yuqing Yao,[a] Hua Jiang,[a] Jing Guo,*[a] Andrzej Rajca,*[b] Ying Wang*[a]*

[a] College of Chemistry, Beijing Normal University, Beijing 100875, China
[b] Department of Chemistry, University of Nebraska, Lincoln, NE 68588–0304, USA
[c] Institute of Chemistry, Chinese Academy of Sciences, Beijing 100190, China

* Corresponding authors:
Hua Jiang, email: jiangh@bnu.edu.cn
Jing Guo, email: jguo1294@bnu.edu.cn
Andrzej Rajca, email: arajca1@unl.edu
Ying Wang, email: ywang1@bnu.edu.cn

Abstract: The design of organic materials with narrow electrochemical gaps (E_{gap}) is critical for modern electronics, yet achieving such narrow gaps while retaining robust stability and facile processability remains a fundamental challenge. Herein, we report a new strategy based on targeted attenuation of aromaticity in π-extended Blatter-type radicals that enables notable gap reduction to 0.75 eV—the lowest reported for this class. We prepare the robust Blatter radical derivatives **1** and **1-tBu**, in which its triazinyl moiety is fused with the central ring of phenanthrene, creating an annulated ring system with reduced aromaticity, compared to classical Blatter radicals. Our studies indicate that reducing fusion-ring aromaticity lowers substantially the gas-phase ionization potential while moderating neutral-state solvation enhancement that typically accompanies π-extension, thereby preserving larger differential solvation stabilization and consequently a substantial E_{gap} reduction. Experimental E_{gap} is observed to exhibit high correlation with the DFT-computed total spin density on the triazinyl-fused ring for the studied Blatter derivatives. In addition, sublimable **1** forms well-ordered thin films of intact radicals on Au(111) surface, highlighting its practical processability. This work establishes aromaticity modulation as an effective strategy for stable, narrow-gap materials, based upon neutral radicals.

Introduction

Rational design of robust organic functional materials with fully reversible redox properties and narrow electrochemical gaps[1] (E_{gap}) is paramount for advancing many next-generation organic electronic devices. For the symmetric cell batteries in which the energy density is less important, optimizing E_{gap} to a minimum would provide an advantage, as it intrinsically enables higher energy efficiency and superior rate capability through lower overpotentials and faster kinetics.[2, 3] To some extent, narrower gaps also may facilitate ambipolar transport in transistors by lowering injection barriers and increasing carrier mobility[4] — properties that are foundations for emerging technologies such as neuromorphic computing[5,6], complementary logic circuits[7] and flexible electronics[8].

Substantial research has been focused on narrowing the HOMO–LUMO energy gap,[9–12] while investigations aimed at reducing the E_{gap} remain significantly underrepresented. It's noteworthy that HOMO–LUMO gap is an orbital-level descriptor for molecules in ground-state geometry, whereas E_{gap} reflects the difference in free energy between different charge states, involving not only orbital energetics but also complex electron reorganization and environmental (solvation) effects. Therefore, strategies developed for tuning HOMO–LUMO gaps do not necessarily translate to the control of E_{gap}. Currently, the primary strategies in reducing the E_{gap} involve π-conjugation extension,[13] utilizing substituent effect,[14] and incorporation of heteroatoms[15,16] (Fig. S1). Nevertheless, these strategies rarely achieved ultranarrow electrochemical gaps (<1.0 eV) for close-shelled systems, and likely encountering synthetic difficulties or a loss of reduction[15,17] and/or oxidation[15,18] reversibility.

Mixed-valence (MV) systems tend to have narrow electrochemical gaps (< 0.6 eV), for which the charge delocalization across the identical redox sites and the whole highly π-conjugated bridge(s), significantly stabilizing the first redox state and reducing the energetic costs of the subsequent electron transfers (Fig. 1).[19–22] For example, we have reported a bis[5]diazahelicene incorporating dihydrazine moiety that possesses an E_{gap} of 0.60 eV for the radical cationic species.[19] Very recently, Shimizu and Matsuda et al. reported the radical cation of a phenanthrene-based Blatter-type diradical that has an E_{gap} = 0.26 eV.[20] Other examples include mixed-valence systems generated from the oxidative or reductive doping of their closed-shell precursors, such as squaraine[23], tetrathiafulvalene (TTF)[24], and perylene-bisimide (PBI)-type[25] molecules. Radical cations with SOMO−HOMO energy level inversion (a violation of the Aufbau principle) exhibit advantages in achieving further reduction of E_{gap}, as the second electron is removed from the energetically more accessible HOMO, resulting in a smaller potential difference (Fig. 1).[26–29] We

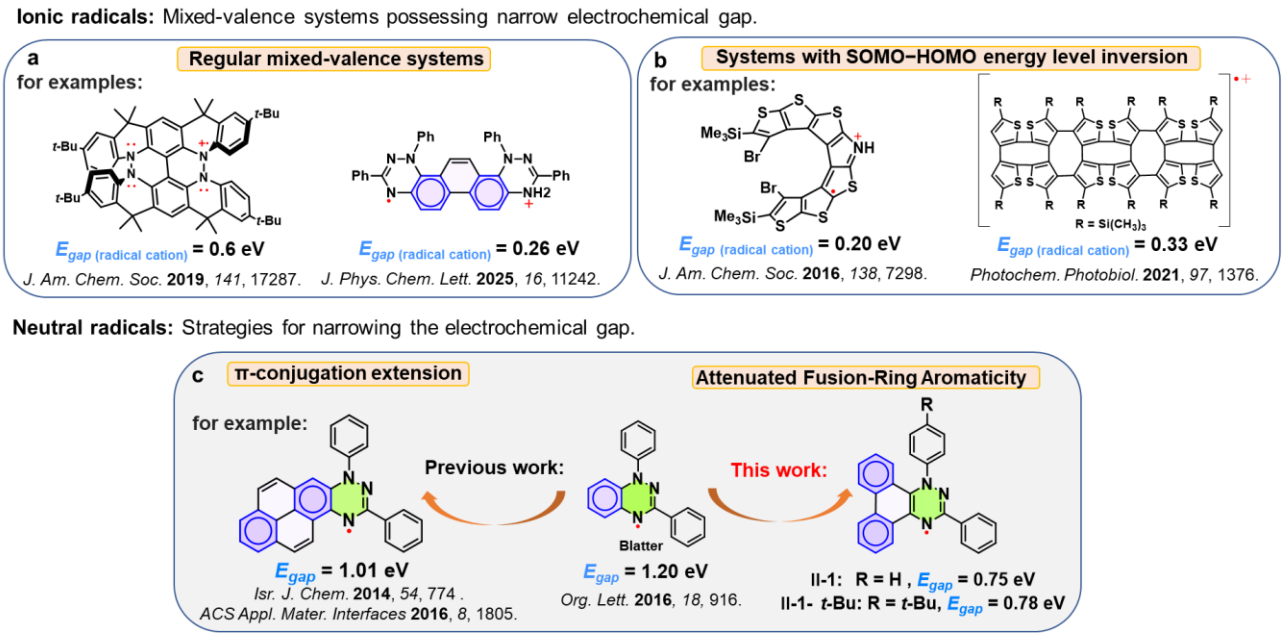


Fig. 1 | Radical systems with narrow electrochemical gaps and strategies for narrowing the gap of neutral radicals. a, Mixed-valence systems have typically narrow E_{gap} due to the charge delocalization across redox sites and π-bridge, stabilizing the first redox state and lowering subsequent transfer costs; **b,** Radical cations with SOMO–HOMO inversion offer advantages for further E_{gap} reduction by removing the second electron from the lower HOMO to minimize the potential difference; Nevertheless, practical application for these species is hindered by their insufficient stability, unfavorable intermolecular packing, and difficulty in sublimation for high-quality thin films. **c,** Strategies used for narrowing E_{gap} of neutral Blatter radicals.

had reported a radical cation of aza-thia[7]helicene with E_{gap} of as low as 0.20 eV;[26] the radical cation of a thiophene-based double helices, for which the energy level of SOMO lies below the four HOMOs, has E_{gap} = 0.33 eV.[28] Nevertheless, the application of the radical ions in devices such as symmetric batteries and transistors remains far from practical, as they themselves and those in higher-charged states are often insufficiently stable. Their intermolecular packing tends to be less favorable for achieving desirable semiconductor band structures due to the presence of "inert" counterions. Furthermore, the sublimation or evaporation of such charged species are challenging, complicating the formation of high-quality thin films.

Neutral, robust organic radicals offer distinct advantages due to their inherent stability and charge neutrality, facilitating sublimation and controlled thin-film growth to enable more efficient charge transport and improved device performance. In this context, benzo[e][1,2,4]triazinyls, also known as Blatter radicals,[30–56] have garnered significant attention for their robust stabilities in three different states of charge (neutral, cationic and anionic) and the highly reversible redox activity,[47]

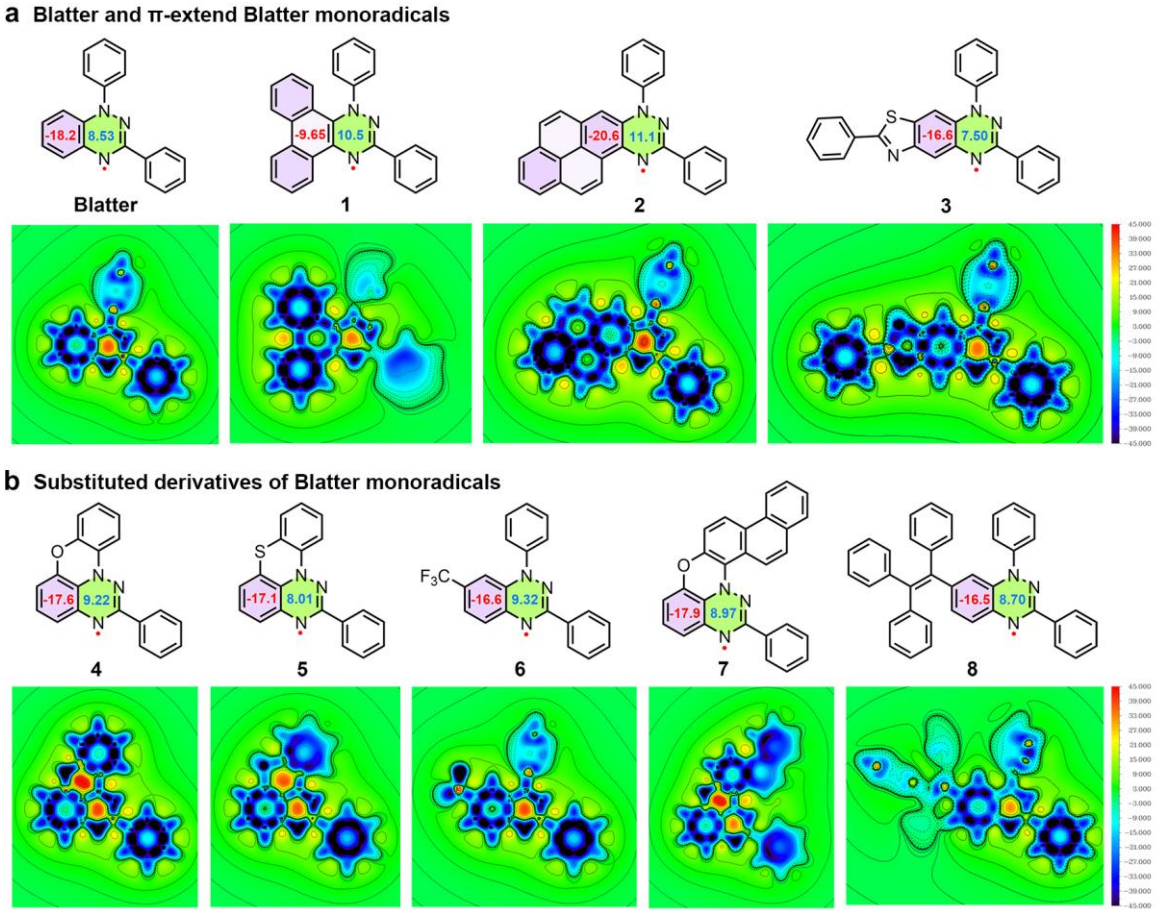


Fig. 2 | Structures and NICS (NICS(1)$_{zz}$ and 2D-NICS) analysis for Blatter radical and its representative monoradical derivatives. These derivatives can be primarily classified into two categories: **a,** fused-ring π-extended derivatives; **b,** substituted derivatives, including π-planarized ones. The values shown in the chemical structures represent the NICS(1)$_{zz}$ (ppm) of the triazinyl (blue numbers) and its fused 6-membered rings (red numbers).

endowing this class of molecules with special potential in semiconductors,[48] redox-flow batteries,[47] NIR photodetectors[54] and metal-free magnet films[43,44,50].

Benzo[*e*][1,2,4]triazinyl has E_{gap} of approximately 1.20 eV. Current efforts to minimize this E_{gap} are focused predominantly on π-extension (**2** and **3**, Fig. 2),[34,35,43] peripheral substitution (mostly represented by **4** – **8**, Fig. 2)[36–42] or π-planarization (**4**, **5** and **7**)[36–38,41]. Although π-extension reduces the gap to some extent (ΔE_{gap} = 0.19 eV for **2**, Table 1), its efficacy plateaus, while the substituent effects as well as π-planarization exhibits marginal impact on gap levels (<0.07 eV, Table 1).

Recent studies show that aromaticity associates tightly with local currents[57] and orbital energy levels[58] of molecules. However, the role of local aromaticity, especially such as that at the triazinyl ring and its fused aromatic ring system where the unpaired electron predominantly resides for

Table 1 | Spin Density as well as Experimental and Computational[a] Redox Potentials for Blatter Radical and Its Derivatives: Total Spin Density on the Triazinyl-Fused Rings (ρ_{FR}, a.u.)[b]; Experimental Oxidation ($E_{1/2}^{0/+1}$, V)/Reduction ($E_{1/2}^{-1/0}$, V) Potentials,[c] Experimental Electrochemical Gaps (E_{gap}^{Expt}, eV); Calculated Oxidation (E_{ox}, eV)/Reduction (E_{red}, eV) Potentials, Calculated Electrochemical Gaps (E_{gap}^{Calc}, eV); Gas-phase Ionization Potential (IP_{gas}, eV), Electron Affinity (EA_{gas}, eV) and Differential Solvation Stabilization ($\Delta\Delta G_{solv}$, eV).

Species	ρ_{FR}	$E_{1/2}^{0/+1}$	$E_{1/2}^{-1/0}$	E_{gap}^{Expt}	E_{ox}	E_{red}	E_{gap}^{Calc}	IP_{gas}	EA_{gas}	$\Delta\Delta G_{solv}$
Blatter	0.184	0.28	–0.92	1.20	4.73	3.34	1.39	6.22	1.83	3.00
1	0.295	0.09	–0.66	0.75	4.51	3.48	1.03	5.86	2.07	2.76
1-*t*Bu[d]	0.290	0.06	–0.72	0.78	—	—	—	—	—	—
2[e 34]	0.217	0.12	–0.89	1.01	4.64	3.44	1.20	5.93	2.15	2.58
3[35]	0.177	0.20	–0.86	1.06	4.78	3.44	1.35	6.07	2.07	2.66
4[36–38]	0.159	0.31	–0.87	1.18	4.78	3.33	1.44	6.29	1.83	3.01
5[36]	0.171	0.33	–0.80	1.13	4.83	3.49	1.34	6.32	2.00	2.98
6[39,40]	0.204	0.42	–0.77	1.19	4.94	3.54	1.40	6.51	2.21	2.91
7[e 41]	0.151	0.41	–0.74	1.15	4.74	3.41	1.34	6.13	2.00	2.80
8[e 42]	0.208	0.42	–0.81	1.23[f]	4.67	3.35	1.32	5.87	2.00	2.56

[a] Carried out at the SMD M06-2X-GD3/def2-TZVP level of theory. [b] The total spin density that distributed on the six atoms of the triazinyl-fused six-membered rings. [c] Cyclic voltammograms of **1**, **1-*t*Bu**, and **Blatter** are shown in Fig. 6b and Figs. S12–21, SI. The electrochemical data of **2**–**8** are from the literature. For radical **4** and **6**, where multiple literature values show slight variations, the values reported herein represent the average of those reported. The electrochemical data for **Blatter** and **2**–**8** reported in the literature, along with the relevant experimental details, are summarized in Table S2. [d] DFT electrochemical calculations were not performed for this derivative. [e] Calculated from the literature. [f] Likely overestimated due to a reduction wave indicative of a multi-electron process.

Blatter radicals, has never been explored as a design parameter for E_{gap} control. This knowledge gap presents an untapped opportunity for radical engineering.

Based on Clar's Rule and extensive experimental evidence,[59] the fused aromatic rings can be broadly categorized into two types: (i) Clar sextets, which possess a fully delocalized 6π-electron system that confers strong aromaticity, leading to exceptional stability and characteristic magnetic properties; (ii) non-Clar rings, which have lower and more localized π-electron density and lack a full aromaticity.[60] In the derivatization of Blatter radicals, the traditional π-extension strategy focuses on fusing the triazinyl ring to a strong aromatic ring (a Clar sextet) to enhance electronic delocalization. In contrast, we seek to tune the redox properties by utilizing the distinct electronic properties of the non-Clar rings.

Here we report highly stable phenanthrene-fused triazinyl radicals **1** and **1-*t*Bu** that achieve the narrowest E_{gap} ever recorded for this class (E_{gap} = 0.75 eV), significantly surpassing all their known π-extended and substituted analogues. Our combined experimental and computational analysis reveals that these radicals attain aromaticity reduction in the triazinyl-fused six-membered ring, which narrows the E_{gap} *via* an effective reduction of the gas-phase ionization potential and a

moderated enhancement of neutral-state solvation compared to conventional π-extension strategy. The E_{gap} is observed to show a strong correlation with the total spin density at the triazinyl-fused six-membered ring in the studied cases. Radical **1** is readily sublimed under high-vacuum thermal evaporation at a controlled source temperature (123–127 °C) to form well-ordered thin films, paving the way for its application in organic spintronics.

Results and Discussion

Synthesis

The classical routes to aryltriazinyl radicals via amidrazones were often suffered from intermediate instability.[30,31,61] In this regards, significant advances were made by Koutentis, et al., who have developed two efficient approaches to access privileged *N*'-aryl-*N*'-[2-aminophenyl]hydrazides intermediates: i) S_NAr of 1-fluoro(chloro)-2-nitrobenzenes with hydrazides followed by nitro reduction,[62] and ii) copper-mediated C–N coupling between 2-iodoanilines and hydrazides.[63] Subsequent cyclization and oxidation afford the benzotriazinyl radicals. For our system, considering the ready availability of the starting material, we envisioned that 9-bromo-10-nitrophenanthrene could serve as a suitable substrate for a Pd-catalyzed coupling to access the key *N*'-(10-aminophenanthren-9-yl)hydrazide intermediate.

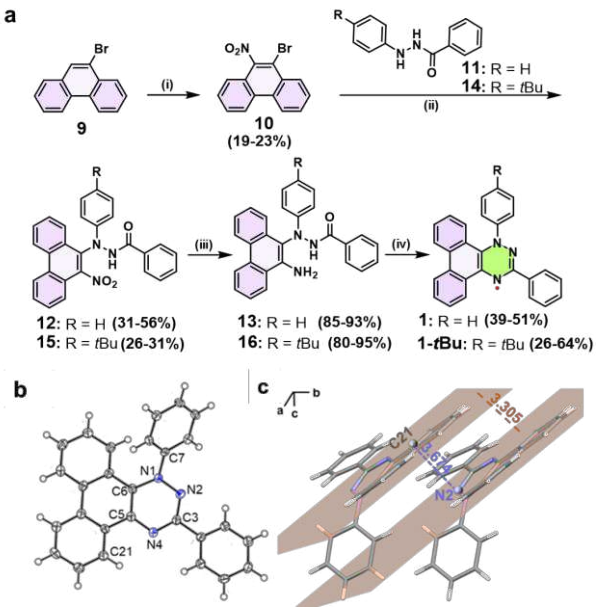


Fig. 3 | Synthetic routes and X-ray structure. a, Synthetic routes to **1** and **1-*t*Bu**. (i) Ac_2O, HNO_3, r.t., 12 h; (ii) $Pd_2(dba)_3$, dppf, *t*-BuONa, Ac_2O, toluene, 100 °C, 12 h; (iii) 10% Pd/C, $HCOONH_4$, EtOH, 90 °C, 3 h; (iv) AcOH, 118 °C; then 2 M NaOH, air, r.t.. **b,** X-ray molecular structure of **1**; Atoms are depicted with thermal ellipsoids set at the 50% probability level. **c,** Paired packing of **1** into columns along *b* direction of slipped π–π stacking of the phenanthrene moiety.

The synthetic routes for **1** and its *tert*-butyl derivative **1-*t*Bu** are shown in Fig. 3a. Initially, the nitration of commercially available 9-bromophenanthrene (**9**) gave **10**. A subsequent Buchwald-Hartwig reaction with benzoyl hydrazide **11** provided **12**. The nitro group was then catalytically hydrogenated, using ammonium formate as hydrogen donor, to obtain **13**. Finally, acid-catalyzed cyclization of **13**, followed by aerobic oxidation under a basic condition, yielded the target radical **1**. Radical **1-*t*Bu** was prepared analogously.

X-ray Crystallography

Crystals of **1** suitable for X-ray crystallography were obtained by slow diffusion of *n*-pentane into ethyl acetate solutions (Fig. 3b–c). The crystal is a monoclinic system, with space group of $P2_1$. The X-ray structure shows a predominantly planar geometry for the phenanthro[9,10-e][1,2,4]triazinyl unit overall. Due to steric hindrance between the phenyl group at N1 and the phenanthrene moiety, the triazine ring exhibits a slight distortion from planarity, with the dihedral angle of 9.0° between the plane of N1, N2, and C3 and that of C6, C5 and N4 (Fig. 3b).

Radical **1** forms 1D chains via π-π interactions in which the molecules are related by translation along the *b*-axis, with a closest interplanar distance of 3.31 Å and short intermolecular contacts (e.g., N2···C21 = 3.67 Å)[64] (Fig. 3c, Fig. S4 and Table S13).

Stabilities

Both **1** and **1-*t*Bu** show excellent stability at ambient conditions. In addition, comparable robust thermal stability for these two radicals is determined by thermogravimetric analysis (TGA) data.

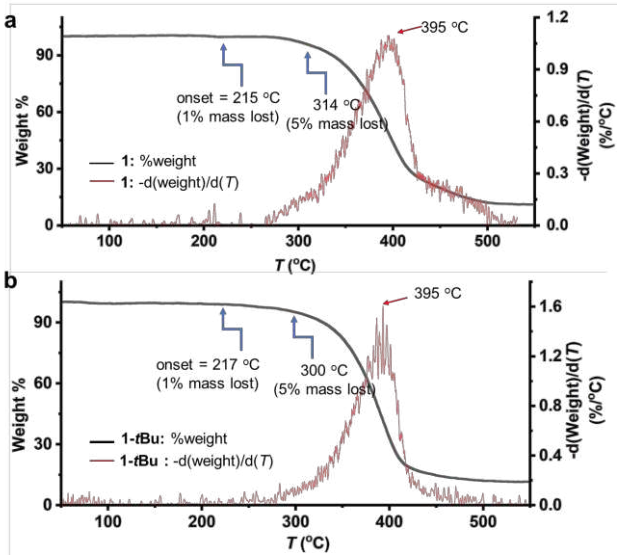


Fig. 4 | Thermogravimetric analysis. Thermogravimetric analysis (TGA) of **a, 1** and **b, 1-*t*Bu** under N_2; heating rate = 5 °C min^{-1}.

The onsets of thermal decomposition, corresponding to a 1% mass loss, are measured at 215 °C for **1** and 217 °C for **1-*t*Bu** (Fig. 4). The temperature corresponding to 5% mass loss is 314 °C for **1** and 300 °C for **1-*t*Bu**, representing an enhanced thermal robustness in comparison with our previously reported pyrene-fused triazinyl radical **2** (5% mass loss at 250 °C).[43]

UV-vis-NIR and EPR Spectroscopies and Electrochemistry

UV-vis-NIR spectra of **1** and **1-*t*Bu** in CH_2Cl_2 exhibit a very similar pattern, which consist of two main absorption bands with maxima at around 257 and 316 nm. A broad shoulder peak appears in the range of 375–468 nm and the longest wavelength absorption bands at approximately 600–1000 nm, characterized by broad absorption envelopes (Fig. 5 and S7). A linear Beer–Lambert plot (R^2 = 0.999) obtained for **1** in DCM over a range of 0.008–1.0 mM (Fig. S9) suggests a monomeric dispersion of the radicals in solutions.

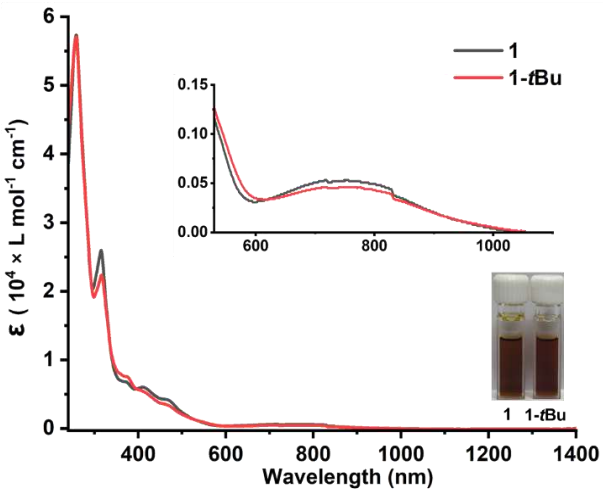


Fig. 5 | UV-vis-NIR absorption spectra. UV-vis-NIR absorption spectra of **1** (2.8×10^{-5} M) and **1-*t*Bu** (3.2×10^{-5} M) in CH_2Cl_2. Inserts: Zoom of the spectra at λ = 570–1200 nm as well as the picture of the samples in the UV cells under the regular condition.

The room-temperature EPR spectra of **1** in DCM and **1-*t*Bu** in toluene display characteristic signatures of Blatter-type radicals (Fig. 6a), with a *g*-value of about 2.003 and a similar splitting pattern due to ^{14}N hyperfine coupling to three nitrogen atoms. The ^{1}H hyperfine couplings are unresolved.

Voltammetry for the radicals in dichloromethane at 25 °C revealed fully reversible redox couples (Fig. 6b and S12). For a 1 mM solution of radical **1**, at a scan rate of 100 mV s^{-1}, well-defined waves were observed at $E_{1/2}^{0/+1}$ = 0.09 V and $E_{1/2}^{-1/0}$ = –0.66 V (*vs* SCE), yielding an experimental

electrochemical gap, E_{gap}^{Expt} = 0.75 eV (Table 1). **1-*t*Bu** displayed comparable behavior, with $E_{1/2}^{0/+1}$ = 0.06 V, $E_{1/2}^{-1/0}$ = –0.72 V and corresponding E_{gap}^{Expt} = 0.78 eV.

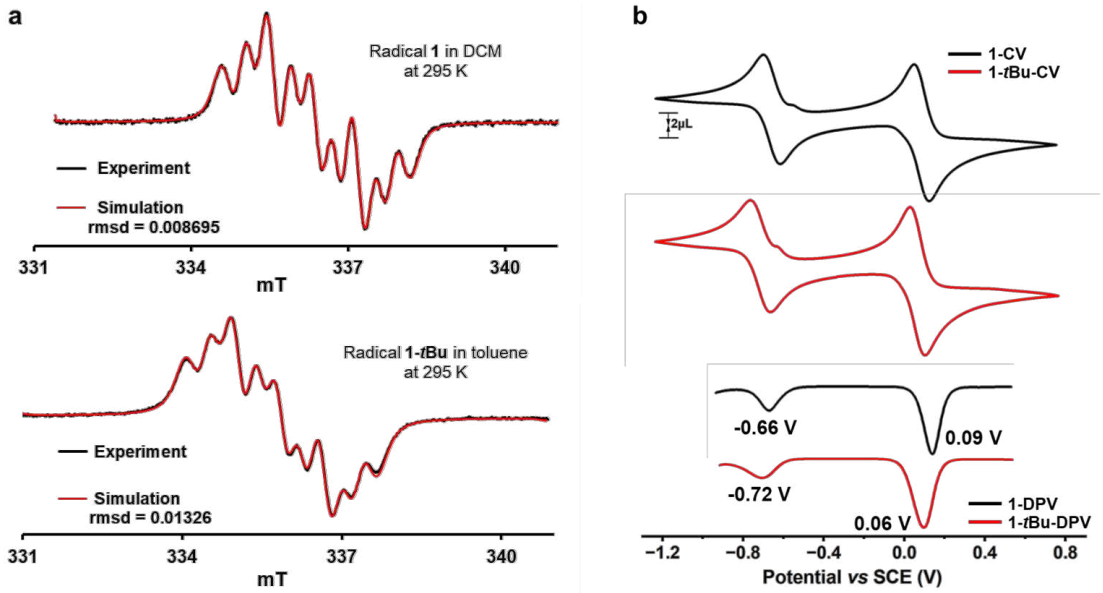


Fig. 6 | EPR Spectroscopies and Electrochemistry. X-band EPR spectra of **a, 1** in DCM (υ = 9.4300 GHz; 0.15 mM) and **b, 1-*t*Bu** in toluene (υ = 9.4168 GHz; 0.20 mM) at 295 K. The ^{14}N hyperfine coupling constants (MHz) are as follows: for **1**, 21.9, 12.6, and 11.8, and for **1-*t*Bu**, 21.8, 13.0, and 11.2. Both spectra are simulated with *g*-values of 2.003 and Voigt line shapes, with a major Lorentzian contribution. **c,** Cyclic voltammetry (CV, up figures) and differential pulse voltammetry (DPV, down figures) of radicals **1** (1 mM) and **1-*t*Bu** (1 mM) in dichloromethane containing *n*-Bu_4NPF_6 (0.1 M) as an electrolyte. Reference electrode = Ag/AgCl; scan rate = 100 mV s^{-1}; temperature = 25 °C. Fc/Fc^+ (0.46 V) was used as an internal reference.

Variable scan-rate cyclic voltammetry (50–500 mV s^{-1}) revealed a linear dependence of peak currents (i_p) on the square root of the scan rate ($\nu^{1/2}$) (Fig. S13–S15), alongside scan-rate-independent peak potentials (Fig. S16). Furthermore, concentration-dependent studies (0.2–1.4 mM) shows that the formal redox potentials remained invariant (Fig. S20), while the peak currents scaled linearly with concentration (Fig. S17–S19). The absence of peak potential shifts and the adherence to ideal Nernstian behavior are characteristics of a reversible, diffusion-controlled electron transfer process intrinsic to the monomeric species.[65] This excludes mechanisms involving intermolecular association, such as π-dimerization at the electrode surface, which would manifest as concentration-dependent equilibria.[66,67] Notably, a minor reduction pre-wave (E = –0.58 V for **1** and –0.64 V for **1-*t*Bu**) is observed across the studied concentrations (Fig. S17) but suppressed at scan rates higher

than 150 mV s^{-1} (Fig. S13). We attribute this scan-rate-dependent phenomenon to a minor surface-confined process, likely the reduction of a small population of radicals adsorbed on the electrode, which behave as a minor surface effect that does not impact the bulk electrochemical properties.

Compared to the parent **Blatter** radical (Table 1, E_{gap}^{Expt} = 1.20 eV), **1** shows a reduction of E_{gap} by 0.45 V. Crucially, **1** possesses a 0.26 V smaller E_{gap} than **2** (E_{gap}^{Expt}= 1.01 eV),[34] a representative conventional π-extended Blatter radical.

To the best of our knowledge, the E_{gap} values for **1** and **1-*t*Bu** represent the lowest electrochemical gaps reported to date for any Blatter-type monoradicals, surpassing all known π-extended analogues and substituted derivatives. Remarkably, these gaps may also be significantly lower than those of several other common neutral radicals, including nitroxides (2.17–2.30 eV),[68] verdazyls (0.98–1.02 eV),[69] oxo-verdazyls (1.38 –1.56 eV),[69] tetrazolinyls (0.87–0.94 eV),[64] and dithiadiazolyls (1.45 –1.68 eV).[70]

Density-Functional Theory (DFT) Computations

DFT calculations were carried out for understanding the behavior for these Blatter-type radicals (Part 10, SI).[71] The optimized geometries for the radicals in dichloromethane at the SMD M06-2X-GD3/def2-TZVP level of theory resembled well those in the crystal structures (Fig. 3b, Table S1). Based on these geometries, the $NICS(1)_{zz}$[72] values of the triazinyl rings of all the studied systems, obtained from the GIAO-UB3LYP/6-31g(d,p) computations, are calculated to be largely positive (Fig. 2 and Fig. S30), indicative of a strong antiaromaticity of these moieties. Such antiaromaticities are supported further by the two-dimensional nucleus-independent chemical shift value (2D-NICS) calculations (Fig. 2), which show obvious shielding in the triazinyl rings. In contrast to the triazinyl rings, the triazinyl-fused six-membered rings show aromaticity (Fig. 2). Moreover, the strength of this aromaticity diverges markedly regarding to the correlates with E_{gap}: While the fused ring in **1** shows the weakest aromaticity ($NICS(1)_{zz}$ = –9.65), coinciding with the narrowest E_{gap} among the studied radicals, the one in **2** displays exceptional aromaticity ($NICS(1)_{zz}$ = –20.6), compared to **Blatter** ($NICS(1)_{zz}$ = –18.2).

The SOMO energy levels of both radical **1** and **2** are above the doubly occupied HOMO levels (Fig. S24 and S26), which obey the Aufbau principle.

DFT-calculated ^{14}N hyperfine coupling constants for neutral **1** in DCM show good agreement with the experimental values, with a linear regression yielding R^2 = 0.97 (Table S14), confirming that the observed EPR signals (Fig. 6a) originate from the radicals in the neutral state. Notably, both experimental and DFT-calculated results consistently show that the coupling at N1 is substantially larger than those at N2 and N4 (Fig. 6a and Table S14). This significant disparity gives rise to a 9-

line hyperfine splitting pattern in the EPR spectra of **1** and **1-*t*Bu** (Fig. 6a), which differs from the 7-line pattern in the cases of **Blatter** and **2**.[33,43]

The DFT(M06-2X-GD3/def2-TZVP)-predicted redox potentials and related electrochemical parameters offer mechanistic insights into the modulation of the energy gaps. Methodology of Born-Haber cycle (Scheme S3) was used for the computations, in which the free energies of the oxidation (ΔG_{ox}^{0}) and reduction reactions (ΔG_{red}^{0}) were determined based on the gas-phase ionization potential (IP_{gas}; the enthalpy change between the cationic and neutral molecules) and electron affinity (EA_{gas}; the enthalpy difference between optimized neutral and anionic species), corrected by solvation effects through:

$$\Delta G_{ox}^{0} = IP_{gas} + \Delta G_{sol}(cation) - \Delta G_{sol}(neutral) \qquad (1)$$

$$\Delta G_{red}^{0} = -EA_{gas} + \Delta G_{sol}(anion) - \Delta G_{sol}(neutral) \qquad (2)$$

where ΔG_{sol} denote the solvation free energy for each species.[73,74] The corresponding thermodynamic redox potentials, E_{ox} and E_{red}, were calculated by Faraday's law:

$$E_{ox} = \frac{\Delta G_{ox}^{0}}{nF} \qquad (3)$$

$$E_{red} = \frac{-\Delta G_{red}^{0}}{nF} \qquad (4)$$

where n is the number of electrons transferred (n = 1 in the studies cases) and F is the Faraday constant.

The differential solvation stabilization energy ($\Delta\Delta G_{sol}$), likewise a critical parameter governing redox potential modulation, was obtained by,

$$\Delta\Delta G_{sol} = -\Delta G_{sol}(anion) - \Delta G_{sol}(cation) + 2\,\Delta G_{sol}(neutral) \qquad (5)$$

Therefore, the calculated redox gap, E_{gap}^{Calc}, can be also expressed as,

$$E_{gap}^{Calc} = \frac{1}{nF}(IP_{gas} - EA_{gas} - \Delta\Delta G_{sol}) \qquad (6)$$

As shown in Table 1, the theoretically predicted redox potentials exhibit good consistency with the experimental voltammetry measurements, capturing the key trends despite a systematic deviation of approximately 0.20 eV. Relative to **Blatter** (E_{gap}^{Calc} = 1.39 eV), both **1** (E_{gap}^{Calc} = 1.03 eV)

and **2** (E_{gap}^{Calc} = 1.20 eV) exhibit a lower oxidation potential (E_{ox}) and a higher reduction potential (E_{red}).

The gas-phase ionization potentials (IP_{gas}) decrease relative to **Blatter** (6.22 eV) for all the π-extended systems, with **1** (5.86 eV) exhibiting a more substantial reduction than **2** (5.93 eV), indicating a lower energy cost for oxidation.

In both **1** and **2**, the extensive π-conjugation delocalizes the positive charge across the expanded framework, which stabilizes their cations relative to the Blatter analogue. This common π-extension effect provides the foundational reduction in IP_{gas} for both systems.

The superior performance of **1** may arise from an additional factor, i.e., the attenuated aromaticity of its fused ring, which results in an inherently less stable neutral molecule, thereby elevating the initial energy level of the reactant. Consequently, oxidation of **1** proceeds from this high-energy baseline, requiring less energy input to reach the stabilized cationic state. For **2**, while π-conjugation also stabilizes the cation, its neutral molecule is pre-stabilized by a strongly aromatic pyrene-fused ring, resulting in a larger energy gap to overcome upon oxidation. Notably, the attenuated aromaticity in **1** may also increase the reorganization energy associated with oxidation, thereby raising the kinetic barrier and contributing to its oxidative stability despite the narrow electrochemical gap.

The gas-phase electron affinities increase for all π-extended systems relative to **Blatter** (EA_{gas} = 1.83 eV), confirming the enhanced stability of their anionic states due to improved charge delocalization over the larger π-surface. Radical **2** exhibits the highest EA_{gas} (2.15 eV), which is consistent with its extensive, strongly aromatic pyrene moiety serving as an excellent electron-accepting platform. Radical **1** also benefits from π-extension, achieving a raised EA_{gas} of 2.07 eV. The slightly lower EA_{gas} of **1** compared to **2** is probably attributed to the less efficient charge delocalization in the phenanthrene-fused system, limiting anion stabilization despite the destabilization of the neutral state.

Relative to **Blatter** (3.00 eV), **1** – **3** all exhibit decreased $\Delta\Delta G_{sol}$, indicating that π-extension reduces the disparity between the solvation energies of neutral and charged species. The most substantial reduction is observed for **2** (2.58 eV), while **1** shows a comparatively modest decrease to 2.76 eV (Table 1). A closer examination of the solvation energy components (Table S20–21) reveals that, although the solvation of the charged species dominates the absolute solvation energetics of each radical (with $\Delta G_{sol}(cation)$ and $\Delta G_{sol}(anion)$ typically below −2.3 eV, compared to $\Delta G_{sol}(neutral)$ above −1.1 eV), the tuning of $\Delta\Delta G_{sol}$ upon structural modification is governed primarily by enhancement in solvation of the neutrals. For example, in the case of **2**, twice the

differential neutral solvation relative to **Blatter**, $2\Delta\Delta G_{sol}(neutral)$, amounts to −0.56 eV, whereas $\Delta\Delta G_{sol}(cation)$ and $\Delta\Delta G_{sol}(anion)$ are only ca. −0.07 eV. Notably, this solvation enhancement is attenuated for neutral **1** ($2\Delta\Delta G_{sol}(neutral)$ = −0.39 eV). Consequently, the overall differential solvation stabilization energy, $\Delta\Delta G_{sol}$, remains higher in **1** compared to the conventional π-extended systems such as **2**.

Although the establishment of a quantitative relationship between aromaticity and solvation energetics remains challenging in our study, we notice that previous studies have suggested that reducing aromaticity can limit molecular polarizability by localizing π-electrons.[75–77] Besides, we observe a strong correlation (R^2 = 0.97) between the computed polarizabilities and ΔG_{sol}(neutral) for the studied radicals (Fig. S29). We therefore speculate that, in radical **1**, the attenuated aromaticity of the fused ring limits the increase in polarizability upon π-extension, thereby tempering the enhancement of neutral solvation and preserving a larger $\Delta\Delta G_{sol}$ compared to **2**.

Substituent effects and π-planarization exhibit limited overall impact on E_{gap}^{Calc}, as they induce only small to modest changes in IP_{gas} and EA_{gas}, which often counteract each other, and exert minimal influence on $\Delta\Delta G_{sol}$ (Table 1).

Collectively, our data indicate that the π-extension narrows the electrochemical gap by reducing the gas-phase ionization potential and increasing the electron affinity, yet it also enhances neutral-state solvation, which diminishes $\Delta\Delta G_{sol}$ and partially offsets the net gap reduction. However, the aromaticity reduction strategy offers two additional advantages in narrowing E_{gap}: (i) a more substantial reduction in gas-phase ionization potential, and (ii) a moderation of the enhancement of neutral-state solvation, thereby preserving a larger $\Delta\Delta G_{sol}$.

The identification of a simple structural parameter that correlates with electrochemical gaps could greatly facilitate the design of new radicals. We evaluated several electronic structure parameters and found that the experimentally determined electrochemical gaps (E_{gap}^{Expt}) show strong correlation with the total spin density on the atoms of the triazinyl-fused ring (ρ_{FR}) (Fig. 7 and S33–34), especially when a presumable "outlier", **6**, is excluded (adjusted R^2 = 0.91, Fig. 7). When the correlation is restricted to the π-extended (**1**, **1-*t*Bu**, **2**, **3**) and π-planarized (**4**, **5**, **7**) derivatives, the R^2 value further improves to 0.98 (Figure S34). Compound **8** is omitted from this correlation because of its reduction wave suggesting a multi-electron process,[42] which would lead to an overestimated electrochemical gap, a conclusion supported also by the statistical analysis (Fig. S31–32).

The physical organic basis for this correlation may be rationalized by considering the dual role of spin density distribution. On one hand, it reflects the π-delocalization extent through spin

population across the conjugated backbones; on the other hand, it captures aromaticity reduction via enhanced spin localization in the fused six-membered rings, as a weakened aromatic character permits enhanced spin localization. (Localizing significant spin density on a highly aromatic ring will disrupt its optimal cyclic π-electron delocalization, incurring a substantial penalty from the loss of aromatic stabilization energy.) Radical **6** somewhat deviates from the trend, with the corresponding absolute values of standard residuals = 2.0 (Fig. S33), presumably due to their distinct substituent effects. Future work on expanded datasets may enable the development of a more comprehensive model that incorporates substituent-based correction terms.

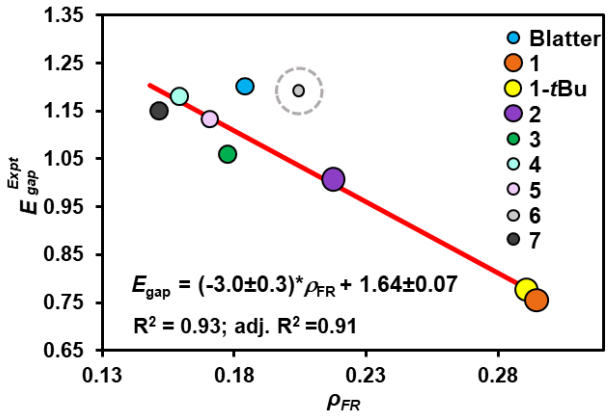


Fig. 7 | Correlation between electrochemical gap and ring spin density. Correlation between the experimentally determined electrochemical gaps (E_{gap}^{Expt}) and DFT-computed total spin density on the triazinyl-fused six-membered ring (ρ_{FR}), excluding a presumable "outlier", **6**, with absolute values of its standard residual of 2.0; error bars for slope and intercept correspond to 95 % confidence interval, with statistically adjusted R^2 = 0.913.

Thin Films

We next characterized the film-forming[43,44,50] properties of **1**. The radical was deposited onto the Au(111) surface held at 298 K via high-vacuum thermal evaporation at various source temperatures (Fig. 8a). Initial deposition at 108 –115 °C for 2 minutes yielded sparse, isolated molecules primarily localized at step edges (Fig. S36a and b), which is attributed to the lower diffusion barrier there compared to terraces. Evaporation at 123 – 127 °C for 50 seconds resulted in a submonolayer coverage with a disordered arrangement (Fig. S36c). Finally, extending the deposition time to 90 seconds (at 123–127 °C) led to higher molecular coverage and promoted the formation of an ordered monolayer film, with an average intermolecular distance of ca. 21.8 Å (Fig. 8b). Notably, DFT calculations on a molecular pair extracted from the X-ray structure, with an intermolecular

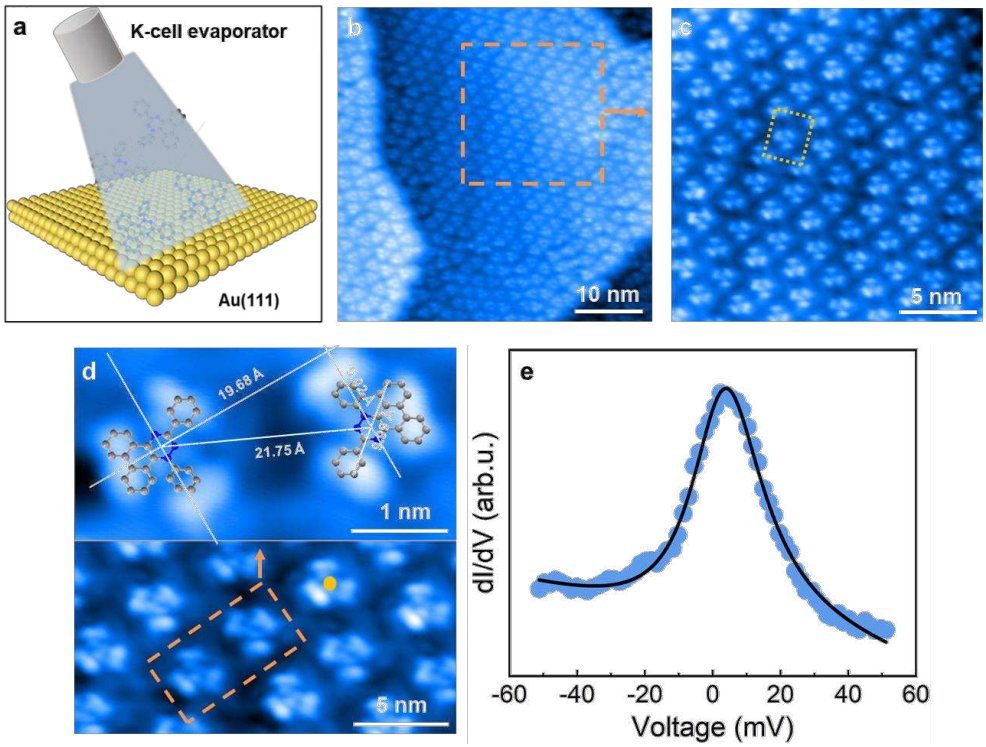


Fig. 8 | Overlayer films of radical 1 on Au(111) surface. a, Schematic of the sample preparation setup. **b, c** Large-scale **b** and close-up **c** STM images of the molecular film (set point: **b** 1 V, 20 pA; **c** 200 mV, 20 pA). The orange dashed rectangle in **b** marks the region shown in **c**. The yellow dashed rectangle in **c** indicates a unit cell, containing one molecule of **1**. **d,** Magnified STM image showing the periodically arranged radical dimers (set point: 100 mV, 20 pA). **e,** *dI/dV* spectrum acquired at the position indicated as the yellow dot shown in **d**, revealing a Kondo resonance. A Fano fit (black solid line) is overlaid onto the experimental data (blue dots). C and N atoms are shown in grey and blue, respectively; H atoms are omitted for clarity.

distance of 14.2 Å, suggest negligible spin-spin coupling and binding between the molecules (Fig. S35 and Table S23). Such interactions are expected to be even weaker at the larger distance observed by STM in the monolayer. As expected, tunneling conductance (*dI/dV*) spectra acquired at the molecular center (yellow spot, Fig. 8d) exhibited a zero-bias peak (ZBP) (Fig. 8e), which can be ascribed to Kondo resonance arising from individual radicals. The resulting line shape of the *dI/dV* can be fit with a Fano function:

$$dI/dV = A + B \cdot (q + \varepsilon)^2 / (1 + \varepsilon^2), \quad \varepsilon = (eV - E_K) / \Gamma \qquad (7)$$

where q reflects the quality of the tip-adsorbate coupling, A and B represent the background and peak amplitudes, E_K is the energy location of the resonance, Γ is the half width at half maximum (HWHM), and e denotes the elementary charge.[46] The fitting (Fig. 8e, solid line) yields the Γ of

12.8 meV and Kondo temperature of 105 K according to the relation, $\Gamma = \sqrt{2}k_BT_K$.[78] Despite possibly being slightly overestimated due to the broadening effects from temperature (6 K), voltage modulation (V_{peak} = 3 mV) and sample voltage noise,[79] as well as the limitation of single-temperature fitting, the obtained Kondo temperature is still much higher than that reported for the thiomethyl-substituted Blatter derivative (26 K)[46] and comparable to that of benzene-ring-linked Blatter triradicals (105/155 K),[80] indicating a high π-coupling efficiency and strong exchange coupling between **1** and the Au(111) surface. The observed asymmetry in the Kondo peak is mainly due to the quantum interference between the unpaired-electron orbital and continuum tunneling channels, which agrees well with previous works.[45,46]

Conclusion

In summary, we report a new design strategy for narrow-gap Blatter-type radicals through targeted attenuation of aromaticity at the triazinyl fusion site, distinct from conventional π-extension approaches that preserve strong aromatic character in the fused ring. We synthesized phenanthrene-fused 1,2,4-triazinyl radicals **1** and **1-*t*Bu**, with the triazinyl moiety specifically annulated to the central ring of the phenanthrene scaffold. These radicals exhibit excellent thermal stability, and achieve recorded-narrow electrochemical gap (E_{gap}^{Expt} = 0.75 eV for **1** and E_{gap}^{Expt} = 0.78 eV for **1-*t*Bu**) among reported Blatter-type monoradicals. NICS calculations confirmed aromaticity reduction at the triazinyl-fused rings compared to the Blatter system. Computational electrochemical studies indicate that the reduced aromatic stabilization of the fused ring within π-extended systems is associated with a more pronounced reduction in gas-phase ionization potential and a moderated enhancement of neutral-state solvation compared to conventional π-extended analogues. In addition, within the studied Blatter derivatives, the total spin density on the triazinyl-fused ring exhibits a strong correlation with the electrochemical gap. The radical **1** forms well-ordered thin films on Au(111) surface under ultrahigh vacuum conditions, with the open-shell configuration of the radicals preserved. This work lays the groundwork for establishing both fundamental principles for designing narrow-gap organic radicals and insights for the practical application of organic radicals in molecular spintronics.

Acknowledgements

This work was supported by the National Science Foundation of China (22371018 to Y.W.; 22271019 and 22471022 to H.J.) and the National Science Foundation of the United States (CHE-

1955349 and CHE-2247170 to A.R.). We thank Dr. Suchada Rajca for contribution to the paper writing.

Conflict of Interests

The authors declare no conflict of interest.

Data Availability Statement

The data that support the findings of this study are available from the corresponding authors upon reasonable request. CCDC 2488806 contains the supplementary crystallographic data for this paper. This data can be obtained free of charge from The Cambridge Crystallographic Data Centre via www.ccdc.cam.ac.uk/data_request/cif.

References

1. Bredas, J.-L. Mind the Gap! *Mater. Horiz.* **1**, 17−19 (2014).
2. Ahn, S., Yun, A., Ko, D., Singh, V., Joo, J. M. & Byon, H. R. Organic Redox Flow Batteries in Non-Aqueous Electrolyte Solutions. *Chem. Soc. Rev.* **54**, 742−789 (2025).
3. Peng, C., et al. Proton-Coupled Chemistry Enabled p–n Conjugated Bipolar Organic Electrode for High-Performance Aqueous Symmetric Battery. *Adv. Funct. Mater.* **34**, 2401001 (2024).
4. Zaumseil, J. & Sirringhaus, H. Electron and Ambipolar Transport in Organic Field-Effect Transistors. *Chem. Rev.* **107**, 1296−1323 (2007).
5. Fuller, E. J., et al. Redox Transistors for Neuromorphic Computing. *IBM J. Res. Dev.* **63**, 9 (2019).
6. Zhu, L., *et al.* Flexible Organic Electrochemical Transistors for Energy-Efficient Neuromorphic Computing. *Nanomaterials* **14**, 1195 (2024).
7. Huang, W., et al. Vertical Organic Electrochemical Transistors for Complementary Circuits. *Nature* **613**, 496−502 (2023).
8. Ji, L., Shi, J., Wei, J., Yu, T. & Huang, W. Air-Stable Organic Radicals: New-Generation Materials for Flexible Electronics? *Adv. Mater.* **32**, 1908015 (2020).
9. Scharber, M. C. & Sariciftci, N. S. Low Band Gap Conjugated Semiconducting Polymers. *Adv. Mater. Technol.* **6**, 2000857 (2021).
10. Cheng, P. & Yang, Y. Narrowing the Band Gap: The Key to High-Performance Organic Photovoltaics. *Acc. Chem. Res.* **53**, 1218−1228 (2020).

11. Zhang, H., Liu, J., Xu, T., Ji, W. & Zong, X. Recent Advances on Small Band Gap Semiconductor Materials (≤2.1 eV) for Solar Water Splitting. *Catalysts* **13**, 728 (2023).
12. Ortstein K., et al. Band Gap Engineering in Blended Organic Semiconductor Films Based on Dielectric Interactions. *Nat. Mater.* **20**, 1407−1413 (2021).
13. Shoyama, K., Mahl, M. Seifert, S. & Würthner, F. A General Synthetic Route to Polycyclic Aromatic Dicarboximides by Palladium-Catalyzed Annulation Reaction. *J. Org. Chem.* **83**, 5339−5346 (2018).
14. Zhang, H., et al. Regulating Energy Band Structures of Triazine Covalent Organic Frameworks with Electron-Donating/Withdrawing Substituents for Visible-Light-Responsive Photocatalytic Tetracycline Degradation and Cr(VI) Reduction. *J. Hazard. Mater.* **446**, 130756 (2023).
15. Kubota, T., Kano, K., Uno, B. & Konse, T. Energetics of the Sequential Electroreduction and Electrooxidation Steps of Benzenoid Hydrocarbons. *Bull. Chem. Soc. Jpn.* **60**, 3865−3877 (1987).
16. Appleton, A. L., et al. Effects of Electronegative Substitution on the Optical and Electronic Properties of Acenes and Diazaacenes. *Nat. Commun.* **1**, 91 (2010).
17. Zhang, P. F., et al. Parent B_2N_2-Perylenes with Different BN Orientations. *Angew. Chem. Int. Ed.* **60**, 23313−23319 (2021).
18. Attwood, M., et al. Asymmetric *N*-heteroacene Tetracene Analogues as Potential n-Type Semiconductors. *J. Mater. Chem. C* **9**, 17073−17083 (2021).
19. Shu, C., Zhang, H., Olankitwanit, A., Rajca, S. & Rajca, A. High-Spin Diradical Dication of Chiral π-Conjugated Double Helical Molecule. *J. Am. Chem. Soc.* **141**, 17287−17294 (2019).
20. Fujimoto, Y., Shimizu, D. & Matsuda, K. Rational Design of a Metal-Free Organic Radical Cation Exhibiting Mid-IR π–π* Transition Based on the Exchange Interaction. *J. Phys. Chem. Lett.* **16**, 11242−11247 (2025).
21. Burrezo, P. M., et al. Bis(aminoaryl) Carbon-Bridged Oligo(phenylenevinylene)s Expand the Limits of Electronic Couplings. *Angew. Chem. Int. Ed.* **56**, 2898−2902 (2017).
22. Euringer, L., et al. Tuning Electron Transfer Coupling and Exchange Interaction in Bis-triarylamine Radical Cations and Dications by Bridge Electron Density. *J. Am. Chem. Soc.* **146**, 27679−27689 (2024).
23. Singh, A., Singh, A. K., Dixit, R., Vanka, K., Krishnamoorthy, K. & Nithyanandhan, J. Visible, Far-Red, and Near-Infrared Active Unsymmetrical Squaraine Dyes Based on Extended Conjugation within the Polymethine Framework for Dye-Sensitized Solar Cells. *ACS Appl. Energy Mater.* **7**, 1461−1475 (2024).
24. Perepichka, D. F., Bryce, M. R., Pearson, C., Petty, M. C., McInnes, E. J. L. & Zhao, J. P. A

Covalent Tetrathiafulvalene-Tetracyanoquinodimethane Diad: Extremely Low HOMO-LUMO Gap, Thermoexcited Electron Transfer, and High-Quality Langmuir–Blodgett Films. *Angew. Chem. Int. Ed.* **42**, 4636−4639 (2003).

25. Sau, A., et al. Mechanistic Investigation of a Photocatalyst Model Reveals Function by Perylene-Like Closed Shell Super-Photoreductant Capable of Reducing Unactivated Arenes. *ACS Catal.* **14**, 2252−2263 (2024).
26. Wang, Y., Zhang, H., Pink, M., Olankitwanit, A., Rajca, S. & Rajca, A. Radical Cation and Neutral Radical of Aza-thia[7]helicene with SOMO–HOMO Energy Level Inversion. *J. Am. Chem. Soc.* **138**, 7298−7304 (2016).
27. Guo, H., et al. High stability and luminescence efficiency in donor–acceptor neutral radicals not following the Aufbau principle. *Nat. Mater.* **18**, 977−984 (2019).
28. Rajca, A., Shu, C., Zhang, H., Zhang, S., Wang, H. & Rajca, S. Thiophene-Based Double Helices: Radical Cations with SOMO–HOMO Energy Level Inversion. *Photochem. Photobiol.* **97**, 1376−1390 (2021).
29. Gao, Y., Liu, Y.-C., & Wu, Y. SOMO-HOMO inversion in Blatter radical derivatives via substituent functionalization. *Chem. Phys. Lett.* **884**, 142593, (2026).
30. Blatter, H. M. & Lukaszewski, H. A New Stable Free Radical. *Tetrahedron Lett.* **9**, 2701−2705 (1968).
31. Gubaidullin, A. T., Buzykin, B. I., Litvinov, I. A. & Gazetdinova, N. G. Molecular and Crystal Structure of a Superstable Free Radical, 1,3-Diphenyl-1,4-dihydro-1,2,4-benzotriazin-4-yl. *Russ. J. Gen. Chem.* **74**, 939−943 (2004).
32. Ji, Y., Long, L. & Zheng, Y. Recent Advances of Stable Blatter Radicals: Synthesis, Properties and Applications. *Mater. Chem. Front.* **4**, 3433−3443 (2020).
33. Constantinides, C. P., Obijalska, E. & Kaszyński, P. Access to 1,4-Dihydrobenzo[e][1,2,4] triazin-4-yl Derivatives. *Org. Lett.* **18**, 916−919 (2016).
34. Zheng, Y., Miao, M. S., Kemei, M. C., Seshadri, R. & Wudl, F. The Pyreno-Triazinyl Radical-Magnetic and Sensor Properties. *Isr. J. Chem.* **54**, 774−778 (2014).
35. Berezin, A. A., Constantinides, C. P., Drouza, C., Manoli, M. & Koutentis, P. A. From Blatter Radical to 7-Substituted 1,3-Diphenyl-1,4-dihydrothiazolo[5′,4′:4,5]benzo[1,2-e][1,2,4]triazin-4-yls: Toward Multifunctional Materials. *Org. Lett.* **14**, 5586−5589 (2012).
36. Kaszyński, P., Constantinides, C. P. & Young, V. G. The Planar Blatter Radical: Structural Chemistry of 1,4-Dihydrobenzo[e][1,2,4]triazin-4-yls. *Angew. Chem. Int. Ed.* **55**, 11149−11152 (2016).
37. Bartos, P., Anand, B., Pietrzak, A. & Kaszyński, P. Functional Planar Blatter Radical through

Pschorr-Type Cyclization. *Org. Lett.* **22**, 180−184 (2019).

38. Hande, A. A., et al. UV-photoelectron spectroscopy of stable radicals: the electronic structure of planar Blatter radicals as materials for organic electronics. *Phys. Chem. Chem. Phys.* **22**, 23637−23644 (2020).
39. Constantinides, C. P., Koutentis, P. A., Krassos, H., Rawson, J. M. & Tasiopoulos, A. J. Characterization and Magnetic Properties of a "Super Stable" Radical 1,3-Diphenyl-7-trifluoromethyl-1,4-dihydro-1,2,4-benzotriazin-4-yl. *J. Org. Chem.* **76**, 2798−2806 (2011).
40. Savva, A. C.*,* et al. Preparation of Blatter Radicals via Aza-Wittig Chemistry: The Reaction of *N*-Aryliminophosphoranes with 1-(Het)aroyl-2-aryldiazenes. *J. Org. Chem.* **82**, 7564−7575 (2017).
41. Zissimou, G. A., Bartos, P., Pietrzak, A. & Kaszyński, P. "Upper" Ring Expansion of the Planar Blatter Radical via Photocyclization: Limitations and Impact on the Electronic Structure. *J. Org. Chem.* **87**, 4829−4837 (2022).
42. Hu, X., Chen, H., Zhao, L., Miao, M. & Zheng, Y. Observation of a Solid-State-Induced Thermally Populated Spin-Triplet State in Radical Regioisomers. *Chem. Mater.* **31**, 10256−10262 (2019).
43. Ciccullo, F., Gallagher, N. M., Geladari, O., Chassé, T., Rajca, A. & Casu, M. B. A Derivative of the Blatter Radical as a Potential Metal-Free Magnet for Stable Thin Films and Interfaces. *ACS Appl. Mater. Interfaces* **8**, 1805−1812 (2016).
44. Ciccullo, F.*,* et al. Interfacing a Potential Purely Organic Molecular Quantum Bit with a Real-Life Surface. *ACS Appl. Mater. Interfaces* **11**, 1571−1578 (2019).
45. Low, J. Z.*,* et al. The Environment-Dependent Behavior of the Blatter Radical at the Metal–Molecule Interface. *Nano Lett.* **19**, 2543−2548 (2019).
46. Patera, L. L., Sokolov, S., Low, J. Z., Campos, L. M., Venkataraman, L. & Repp J. Resolving the Unpaired-Electron Orbital Distribution in a Stable Organic Radical by Kondo Resonance Mapping. *Angew. Chem. Int. Ed.* **58**, 11063−11067 (2019).
47. Steen, J. S.*,* et al. Blatter Radicals as Bipolar Materials for Symmetrical Redox-Flow Batteries. *J. Am. Chem. Soc.* **144**, 5051−5058 (2022).
48. Zhang, Y., Zheng, Y., Zhou, H., Miao, M. S., Wudl, F. & Nguyen, T. Q. Temperature Tunable Self-Doping in Stable Diradicaloid Thin-Film Devices. *Adv. Mater.* **27**, 7412-7419 (2015).
49. Hou, Y., Chen, H., Lian, W., Li, H., Hu, X. & Liu, X. Calamitic Blatter Radicals for Large-Area Solution-Coated Resistive Memories. *Adv. Funct. Mater.* **33**, 2306056, (2023).
50. Nowik-Boltyk, E. M.*,* et al. Radical-Induced Changes in Transition Metal Interfacial Magnetic Properties: A Blatter Derivative on Polycrystalline Cobalt. *Angew. Chem. Int. Ed.* **63**,

e202403495 (2024).

51. Bar-David, J., et al. Electronically Perturbed Vibrational Excitations of the Luminescing Stable Blatter Radical. *ACS Nano* **19**, 7650−7660 (2025).
52. Mitra, G., et al. Conventional Versus Singlet-Triplet Kondo Effect in Blatter Radical Molecular Junctions: Zero-Bias Anomalies and Magnetoresistance. *Chem* **11**, 102500 (2025).
53. Peng, K., et al. Redox Tunable Conjugated Radicals Enable Low Threshold Voltage Memristors for Artificial Synapses. *Mater. Horiz.* **12**, 8667−8675 (2025).
54. Li, H., et al. Diradicaloid Strategy for High-Efficiency Photothermal Conversion and High-Sensitivity Detection of Near Infrared Light. *Adv. Opt. Mater.* **11**, 2300060 (2023).
55. Ji, Y., et al. 77% Photothermal Conversion in Blatter-Type Diradicals: Photophysics and Photodynamic Applications. *Angew. Chem. Int. Ed.* **135**, e202311387 (2023).
56. Bartos, P., Pomikło, D. & Sorenson, K. B. Two Blatter Radicals Face-to-Face: A Constrained Diradical Architecture. *J. Am. Chem. Soc.* **147**, 125−129 (2025).
57. Stuyver, T., Perrin, M., Geerlings, P., De Proft, F. & Alonso, M. Conductance Switching in Expanded Porphyrins through Aromaticity and Topology Changes. *J. Am. Chem. Soc.* **140**, 1313−1326 (2018).
58. Wu, Y., Liu, J., Yang, G., Bin, Z. & You, J. Aromaticity Localization Effects in Polycyclic Aromatic Hydrocarbons for Discovering Narrowband Fluorescence Materials. *J. Am. Chem. Soc.* **147**, 19305−19314 (2025).
59. Clar, E. The Aromatic Sextet. *John Wiley & Sons*, London, New York, Sydney, Toronto, 1972.
60. Solà, M. Forty years of Clar's aromatic π-sextet rule. *Front. Chem.* **1**, 22 (2013).
61. Koutentis, P. & Lo Re, D. Catalytic Oxidation of N-Phenylamidrazones to 1,3-Diphenyl-1,4-dihydro-1,2,4-benzotriazin-4-yls: An Improved Synthesis of Blatter's Radical. *Synthesis* **12**, 2075−2079 (2010).
62. Berezin, A. A., Zissimou, G., Constantinides, C. P., Beldjoudi, Y., Rawson, J. M. & Koutentis, P. A. Route to Benzo- and Pyrido-Fused 1,2,4-Triazinyl Radicals via N′-(Het)aryl-N′-[2-nitro(het)aryl] hydrazides. *J. Org. Chem.* **79**, 314−327 (2014).
63. Constantinides, C. P., et al. A Magnetostructural Investigation of an Abrupt Spin Transition for 1-Phenyl-3-trifluoromethyl-1,4-dihydrobenzo[e][1,2,4]triazin-4-yl. *J. Am. Chem. Soc.* **136**, 11906−11909 (2014).
64. Yang, Z., et al. Thermally Ultrarobust $S = 1/2$ Tetrazolinyl Radicals: Synthesis, Electronic Structure, Magnetism, and Nanoneedle Assemblies on Silicon Surface. *J. Am. Chem. Soc.* **145**, 13335−13346 (2023).
65. Bard, A. J., Faulkner, L. R. & White, H. S. Electrochemical Methods: Fundamentals and

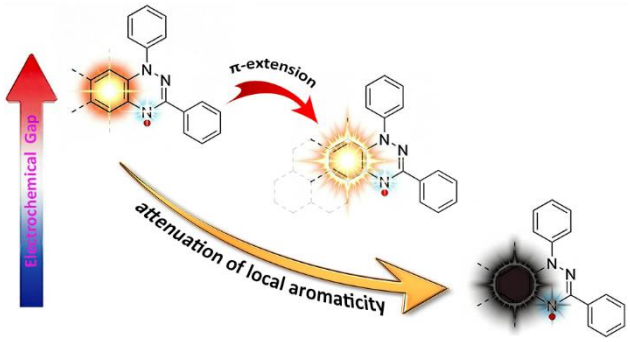
Applications, 3rd Ed. *John Wiley & Sons*, Hoboken, 2022.

66. Xiang, Q., et al. Stable Olympicenyl Radicals and Their π-Dimers. *J. Am. Chem. Soc.* **142**, 11022−11031 (2020).
67. van het Goor, L., van Duijnen, P. T., Koper, C., Jenneskens, L. W., Havenith, R. W. A. & Hartl, F. π-dimerization of pleiadiene radical cations at low temperatures revealed by UV–vis spectroelectrochemistry and quantum theory. *J. Solid State Electrochem.* **15**, 2107−2117 (2011).
68. Salinas, G., Aguilar-Martínez, M. & González, I. Electrochemical Characterization of Stable Nitroxyl Radical, Intermediaries in the Synthesis of 3-Methacryloylamin-PROXYL. *ECS Trans.* **36**, 483−490 (2011).
69. Gilroy, J. B., McKinnon, S. D. J., Koivisto, B. D. & Hicks, R. G. Electrochemical Studies of Verdazyl Radicals. *Org. Lett.* **9**, 4837−4840 (2007).
70. Boere, R. T. & Moock, K. H. Solution Disproportionation Energies of 1,2,3,5-Dithia- and Diselenadiazoles. Direct Comparison of Solution Oxidation Potentials with Ionization Energies in Gas Phase. *J. Am. Chem. Soc.* **117**, 4755−4760 (1995).
71. Frisch, M. J. et al. Gaussian 09, Revision D.01 *Gaussian, Inc.*, Wallingford CT, 2013.
72. Chen, Z., Wannere, C. S., Corminboeuf, C., Puchta, R. & Schleyer, P. v. R. Nucleus-Independent Chemical Shifts (NICS) as an Aromaticity Criterion. *Chem. Rev.* **105**, 3842−3888 (2005).
73. Wang, D., Huang, S., Wang, C., Yue, Y. & Zhang, Q. Computational Prediction for Oxidation and Reduction Potentials of Organic Molecules Used in Organic Light-Emitting Diodes. *Org. Electron.* **64**, 216−222 (2019).
74. Wang, X., Li, F. & Zhang, J. Theoretical Prediction for Redox Potentials of Oxygen-Centered Organic Anions in Aprotic Solvents. *Theor. Chem. Acc.* **142**, 62 (2023).
75. Jartín, R. S., Cuesta, I. G., d. Merás, A. S. & Lazzeretti, P. Can aromaticity be connected with molecular polarizability? A theoretical study of benzene isomers and five-membered heterocyclic molecules. *J. Comput. Methods Sci. Eng.* **4**, 665−676 (2004).
76. Woller, T., Geerlings, P., De Proft, F., Champagne, B. & Alonso, M. Aromaticity as a Guiding Concept for Spectroscopic Features and Nonlinear Optical Properties of Porphyrinoids. *Molecules* **23**, 1333 (2018).
77. Zhang, C., Bell, D., Harger, M. & Ren, P. Polarizable Multipole-Based Force Field for Aromatic Molecules and Nucleobases. *J. Chem. Theory Comput.* **13**, 666−678 (2017).
78. Nagaoka, K., Jamneala, T., Grobis, M. & Crommie, M. F. Temperature Dependence of a Single Kondo Impurity. *Phys. Rev. Lett.* **88**, 077205 (2002).
79. Gruber, M., Weismann, A. & Berndt, R. The Kondo resonance line shape in scanning

tunnelling spectroscopy: instrumental aspects. *J. Phys.: Condens. Matter* **30**, 424001 (2018).

80. Duan, J.-J., et al. Exploiting Structural Flexibility for Reversible Kondo-State Switching in a Pure Organic Radical on Au(111)─Submolecular Imaging and Manipulation. *ACS Nano* **19**, 34981−34989 (2025).

Table of Contents Graphics



Supplementary Files

This is a list of supplementary files associated with this preprint. Click to download.

- CheckCIFforRadical1.pdf
- 20230525DautoRadical1.cif
- SIMay62026YWClean.pdf